Journal of
Materials Chemistry A

Materials for energy and sustainability

Accepted Manuscript

This article can be cited before page numbers have been issued, to do this please use: E. W. Burns, U. Aschauer, M. Döbeli, C. W. Schneider, D. Pergolesi and T. Lippert, *J. Mater. Chem. A*, 2020, DOI: 10.1039/D0TA08117E.

ROYAL SOCIETY OF CHEMISTRY

rsc.li/materials-a

View Article Online
DOI: 10.1039/D0TA08117E

ARTICLE

$LaTiO_2N$ crystallographic orientation control significantly increases visible-light induced charge extraction

Received 00th January 20xx,
Accepted 00th January 20xx

DOI: 10.1039/x0xx00000x

Eric Burns[a,b], Ulrich Aschauer[c], Max Döbeli[d], Christof W. Schneider[a], Daniele Pergolesi[a], Thomas Lippert[a,b,e]

Photocharge extraction in the visible-light energy range is essential to sustain efficient photoelectrochemical processes driven by solar irradiation of photoanode materials. Recent literature has shown that crystallographic orientation can have a significant impact on the extraction of photocharges, though the difficulty of discriminating bulk and surface orientation effects on charge extraction often complicate any understanding as to the role each orientation may play. Our catalyst-decorated thin-film model system allows us to cleanly separate charge extraction limiting effects of bulk vs surface orientation. As a result, our study reveals an anisotropic visible-light induced photocharge extraction dependence on the bulk crystallographic orientation in $LaTiO_2N$ (LTON) photoanodes. In particular, the visible-light induced photocharge extraction is 30% higher for (011) films than (001) oriented thin films. Computational analysis of the LTON band diagram suggests that this is due to a higher potential energy and photocharge mobility along the (011) direction.

Introduction

The world is in the midst of a transition towards environmentally friendly energy alternatives. While sustainable electricity production has matured into a reliable and scalable source of electrical energy, this effort still does not solve the considerable majority of our energy needs which remain in the form of a chemical feedstock (e.g. fuel). One proposed method to provide a sustainable source of fuel is to utilize the largest and most scalable source of renewable energy – our sun – in combination with a direct photoelectrochemical system: *solar fuels*.[1,2]

One of the greatest bottlenecks for the development of efficient solar fuels remains the lack of high-performing photoanode materials for solar fuel production. Most improvements in photoelectrochemical performance are often the result of adjustments to material composition, morphology, or via the introduction of additional material layers. Permutations of these material designs offer steady developments in photoanode efficiency – but often at the cost of added material discovery time or complexity.

Separately, crystallographic orientation control and facet engineering provide a relatively novel and potentially powerful method to optimize *existing* solar fuel materials. Crystallographic orientation is a property inherent to non-amorphous solid-state semiconductors – i.e. most solar fuel materials. Moreover, charge dynamics are often anisotropic and dependent on crystal orientation; by extension, ideal charge extraction for photoelectrochemistry likely also depends on the construction of some optimal internal orientation. Recent experimental studies appear to support this argument and often reveal a tremendous divergence in photocharge extraction along certain crystallographic axes.[3–7] Yet, separate studies complicate this story and indicate that large differences in photocatalytic behavior may be also determined by the presence of catalytically preferred surface facets or surface restructuring.[8,9]

In our work, we adopt the structurally simple single-oriented thin-film model system in order to develop a clearer understanding of the factors affecting photocharge extraction. Our experimental work uses $LaTiO_2N$ (LTON) both because of its ideal bandgap and high reported water oxidation performance.[10–12] Moreover, we hope that the discussion produced via our study can help explain and optimize the performance of LTON photoanodes and that of similar materials in the oxynitride family. To our knowledge, our work for the first time demonstrates a large performance dependency on internal (bulk) LTON crystal orientation. Furthermore, we provide a clear demonstration that bulk crystallographic orientation can play a driving role in photocharge extraction – verifiably separate from surface catalytic behavior. We also report a novel wavelength-dependent photocharge extraction conditional on crystallographic orientation – a feature that may provide the ability to custom-tune the energy of extractable photo charges in solar fuel materials.

Experimental Methods

Materials

[a] Laboratory of Multiscale Materials Experiments, Paul Scherrer Institut, 5232 Villigen, Switzerland
[b] Department of Chemistry and Applied Biosciences, ETH Zürich, Vladimir-Prelog Weg 1-5/10, 8092 Zürich, Switzerland
[c] Department of Chemistry and Biochemistry, University of Bern, Freiestrasse 3, 3012 Bern, Switzerland
[d] Department of Physics, Laboratory of Ion Beam Physics, ETH Zürich, Otto-Stern-Weg 1, 8093 Zürich, Switzerland
[e] Molecular Photoconversion Devices Division, International Institute for Carbon-Neutral Energy Research, Kyushu University, 819-0395 Fukuoka, Japan

View Article Online
DOI: 10.1039/D0TA08117E

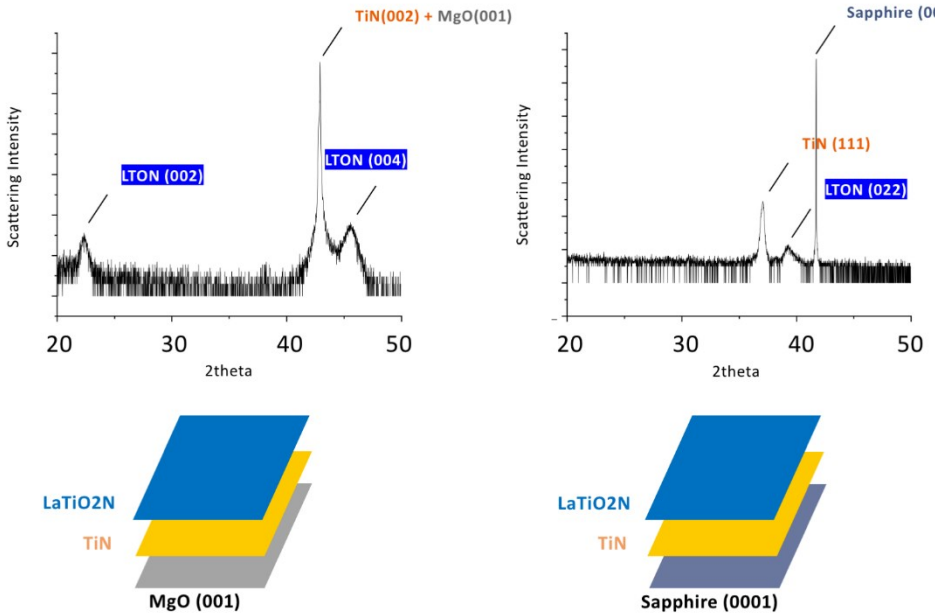

Figure 1. θ-2θ XRD scans of (001) and (011) LTON thin films epitaxially grown on TiN and Mgo (001) or Sapphire (0001) (left and right respectively).

All chemicals were commercially purchased unless noted otherwise.

Sample preparation

Epitaxially-grown thin-film samples were grown via our home-built pulsed laser deposition system on top of (001) MgO and (0001) Al_2O_3 pre-cut 10x10x0.5mm substrates. Samples were prepared in an evacuated chamber with a base pressure of 1 x 10^{-6} mbar using a 248nm (30ns pulse width) KrF excimer laser at 7Hz and an average fluence of 3J/cm^2. The area of the ablation spot was 1mm^2 and the target-to-substrate distance was 55 mm. A 1cm diameter TiN rod target was used for the deposition of TiN on our precut oriented substrates (used as purchased) over a course of 15min and heated to a temperature of 750°C. A homemade 1cm Lanthanum titanium oxide ($La_2Ti_2O_7$) rod target was used in the consecutive deposition of LTON onto epitaxially grown TiN over a course of 30min and heated to a temperature of 750°C. A reactive cross-beam of ammonia gas was injected orthogonally into the plasma plume via steady stream to reach a steady pressure of 2 x 10^{-3} mbar on top of a base pressure of 8 x 10^{-4} mbar nitrogen. Post deposition, samples were cut in half via a dicing saw into samples 10x5x0.5mm in order to ensure identical sample comparisons between catalyst decorated and undecorated samples.

Catalyst deposition

All catalyst depositions were adaptations from prior protocols.[13–15] Nickel oxide (NiO_x) deposition was produced from a 0.85mM $Ni(NO_3)_2$ • 6 H_2O solution at steady voltage -2V vs RHE over 10s.[13] Iridium oxide (IrO_x) solution (for both electrodeposition and dip-deposition) was produced from 0.3mM Na_2IrCl_6 • 6 H_2O and deposited according to prior procedure.[14] Cobalt-phosphate (CoPi) depositions were produced at 1.29 V (*vs.*RHE) in 0.1 M KPi electrolyte at pH 7.0 containing 0.5 mM Co^{2+} over a course of 30min. All catalysts are likely amorphous.

Material analysis

A Seifert diffractometer (Cu, $K_{\alpha 1}$) was used for all theta-2theta and grazing incident measurements to determine all out-of-plane orientations.

The atomic compositions of our thin films were evaluated using by 2 MeV Rutherford backscattering (RBS) and a 13 MeV ^{127}I heavy-ion elastic recoil detection analysis (ERDA) using a time-of-flight spectrometer and gas ionisation detector. A RUMP simulation was used to fit the RBS yield results to produce estimated stoichiometry.

The film thickness was estimated via a calibrated deposition rate using X-ray reflectometry (XRR) measurements of different film thickness. Further, the thickness of both LTON semiconductor and the catalyst layer was calibrated post-experiment via a DEKTAK profilometer.

Photoelectrochemical characterization

Chopped light voltage scans were conducted with an AM1.5 calibrated Newport 100 W Xenon lamp. The light intensity was calibrated prior to each experimental protocol with a Gentech INTEGRA USB power meter. A Metrohm AG µAUTOLAB Type III potentiostat was used as voltage supply and a Nova 11.1 software was used as a programmable interface. PEC measurements were produced using a standard three-electrode (Ag/AgCl reference and Pt wire counter electrode) system in a quartz cell 0.5M NaOH pH13.4 solution. Scanned voltages were post-processed to RHE potentials by using the Nernst equation. JV scans were conducted at a rate of 0.01V/s.

Pulse voltammetry was used to conduct time resolved voltage experiments. A potential of 1.0V was used as a baseline voltage with a pulse voltage of 1.3V.

IPCE measurements were produced using an intensity-calibrated Newport cornerstone monochromator. Photocurrent values were sampled at each 20nm step via a stepwise photo spectrum scan. Constant voltage was applied via the same potentiostat used in the photoelectrochemical setup with an electric current sampling every 0.1s. An estimation of photocurrent was produced via an averaging of points over 1s before and after a jump in current was observed. IPCE values were determined via conversion of current density into energy density divided by incident flux.

Computation

DFT calculations were carried out with the VASP code[16–19] using the PBEsol exchange correlation functional.[20] Electron-nuclear interactions were described by projector augmented-wave potentials with La(5s, 5p, 5d, 6s), Ti(3p, 3d, 4s), O(2s, 2p) and N(2s, 2p) valence states and using a cutoff of 550 eV for the plane-wave basis.[21,22] The virtual crystal approximation (VCA) was used to account for anion disorder, using occupations of ⅓ and ⅔ for N and O on all anion sites. LTON was described as 20-atom orthorhombic cell and all internal and lattice parameters were relaxed with thresholds of 10^{-3} eV/Å for forces and 5×10^{-5} eV/Å^3 for the stress tensor while sampling reciprocal space with a 6×4×6 Monkhorst-Pack mesh, yielding lattice parameters a=5.57 Å, b=7.76 Å, c=5.51 Å and α=β=γ=90.00°.[23] Effective masses were calculated with EMC[24] and k-resolved absorption spectra were calculated via the frequency dependent dielectric tensor[25] and analyzed using the pymatgen wavederf module.[26]

Results and Discussion

We developed singly oriented thin films as a model system in order to investigate possible bulk crystalline orientation roles on charge dynamics. Both out-of-plane (001) and (011) epitaxially oriented LTON thin films were grown using our homemade pulsed laser deposition (PLD) system.

Our material fabrication method is a similar reproduction from our previous work.[8,27] The oxynitride semiconductor is epitaxially grown on top of a conductive titanium nitride (TiN) layer which is also epitaxially grown on top of precut single-crystal MgO (001) or Sapphire (0001) oriented substrates; the purpose of the deposited TiN layer is to provide a conducting back layer for complimentary charge extraction.[8,27] The XRD θ-2θ scans (figure 1), indicates single orientation growth of pseudo-perovskite orthorhombic LTON(001) and (011) on top TiN(001)/MgO(001) and TiN(111)/Al_2O_3(0001) respectively[8]. No resolvable peaks were found in low-angle detector scans and therefore provide evidence of no further in-plane components. Our LTON peaks are noticeably broad. This broad peak feature is evidence of a film consisting of small domains as can be seen in the corresponding AFM and SEM images (figure S1). Comparable LTON film peak widths indicate that domain sizes are similar in both orientations. RBS and ERDA measurements indicate close matching of elemental composition between our LTON oriented samples (figure S2). The films also have comparable thickness. The deposition rate was calibrated via X-ray reflectometry (XRR) and the actual film thickness was verified via profilometer measurements (figure S3). Ultimately, we were able to grow epitaxial thin films, comparable in thickness and composition but different in orientation.

Figure 2 is a current-voltage (JV) plot which shows the photocurrent performance of our two bare photoanode thin films of different orientations (001) and (011) under chopped light illumination. The 'chopped' behavior of our photocurrent is due to the chopped nature of photoanode exposure to full illumination of AM 1.5 irradiation – an abrupt increase in current is due to illumination and an abrupt decrease in current is due to the absence of irradiation. The chopped light illumination allows us to establish the current due to illumination (photocurrent) of our materials. Since current corresponds closely with the extraction of charges, we can treat photocurrent as a measure of photoelectrochemical performance.

Photocurrent differences in the bare (001) and (011) orientation samples appear minimal. The low photocurrent values are due to the lack of catalysts to aid in the extraction of photocharges. Moreover, the extremely smooth surface of our thin films offer a significantly reduced surface area in contrast to most application-based solar fuel studies, as demonstrated in comparative studies, and has a significant dampening effect on photocurrent[28]. However, the flat nature of our films also allows us to produce fair comparisons across samples, where illuminated area corresponds closely with the solid-electrolyte interface area. Our thin film photocurrent values also match the reported range of LTON thin film performances.[8,29] The slightly larger photocurrent observed in LTON (001) aligns well with prior conclusions demonstrating a high absorbed photons-to-current conversion efficiency in bare LTON (001) films.[8] Separately, close observation of our bare LTON films hints at a possible difference in scavengable photocharges evident in the recombination spikes that occur immediately after chopped light (figure 2). These peaks are, on average, larger in LTON (011) (red curve) and may indicate larger initial charge recombination, and therefore may also indicate a larger quantity of potentially scavengable photocharges. Similarly, the larger quantity of available photocharges could support previous work which observes larger photocurrent in (011) films. The (011) surface is also known to be more photoanodic in LTON and other perovskites.[8,30] Nevertheless, since other material features aside from orientation (film thickness, N/O ratio, average grain size) are similar (figures S1 and S2), we can assume that the comparable plateau photocurrents amount to a near-equivalent quantity of photo-charges participating in redox. Therefore, overall water oxidation kinetics between the two oriented bare films must also be similar.

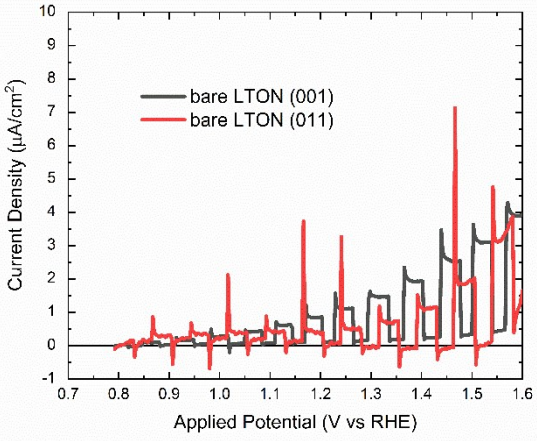

Figure 2. JV scans of bare oriented LTON films under chopped light illumination. Scans were made in pH 13.4 NaOH solution at a scan rate of 0.01V/s from left to right.

However, it can be difficult to resolve bulk crystalline orientation effects of bare LTON films in chopped light JV analysis as it is possible that additional surface charge extraction bottlenecks, such as surface catalytic function and charge extraction, may be masking these differences; in particular, prior work demonstrates surface orientation and termination can also have a significant charge extraction role.[8,31] In order to better separate bulk orientation effects from a possible surface charge extraction bottleneck, we identified an ideal catalyst that could offer similar performance on samples of different orientations. Several electrocatalyst compositions commonly used in solar fuel systems were surveyed (figure 3a).

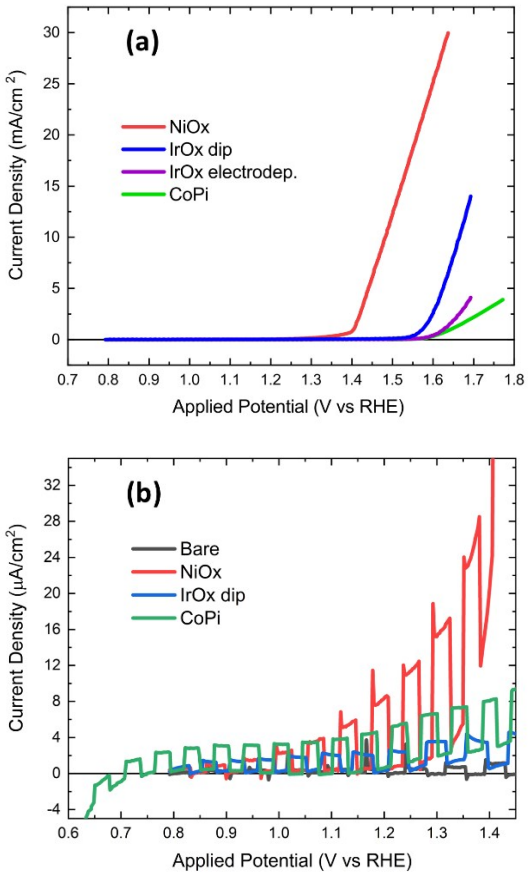

Figure 3. Survey of various water oxidation catalysts for use on LTON photoanodes. a) JV performance of various water oxidation catalysts as deposited onto. FTO. b) JV performance of catalyst decorated LTON (011) photoanodes under chopped light illumination.

Solid-state water oxidation catalysts were first deposited onto conductive fluorine-doped tin oxide substrates and their function as electrocatalysts were studied – their JV curves are visible in figure 3a. Importantly, the JV characteristics of these catalysts exhibit the characteristic sharp irreversible onset curves of water oxidation as well as the absence of any other redox peak. These clean features indicate that there are no other sizable redox side reactions occurring aside from water oxidation. Correspondingly, the studied catalysts remain electrochemically inert over the applied voltage range.

Of the catalysts studied in this work, the nickel oxide catalyst (NiO_x) exhibits the most reductively shifted current onset at ~1.4V (figure 3a). This onset potential rivals state-of-the-art catalysts for water oxidation and also adds a 0.2V reductive advantage over that of the next-best catalyst – the noble metal-based catalyst iridium oxide (IrO_x) (deposited by immersion). Both NiO_x and IrO_x (immersion) catalysts also demonstrate the greatest change in current via applied voltage (i.e. largest slopes). Assuming each catalyst has a 100% water oxidation faradaic yield, then NiO_x and IrO_x (immersion) catalysts demonstrate superior water oxidation kinetics in comparison to the remaining catalysts studied. Intriguingly, (not within the premise of this paper) the catalytic performance of IrO_x behaves vastly different when deposited by immersion versus when electrodeposited.

This same catalytic survey was performed directly on our LTON thin films (figure 3b). Due to the clearly superior photocurrent values in our LTON + NiO_x catalyst system, we chose this system for the remainder of our study.

We performed a series of time-resolved voltage experiments with and without illumination to compare how charges decay over time: data acquisition begins with a voltage switch from 1.0V steady-state to 1.3V (vs RHE). Notably, photo-generated charges decay slower than 'dark' charges generated by the voltage shift, as indicated in the divergence of light and dark decays in figure 4a. This splitting allows us to track both photogenerated charges and 'dark' charges independently via their kinetic decay signature.

Further charge extraction experiments conducted on the oriented LTON-NiO_x samples indicate that catalytic function behaves identically regardless of underlying sample orientation. Comparing the photocharge decay curves (figure 4b) of both oriented LTON + catalyst samples (LTON(001)-NiO_x and LTON(011)-NiO_x respectively) we reveal a close match in their decay signatures. Since the rate of photogenerated charge decay of orientated LTON + catalyst samples is nearly identical over the usual water oxidation time frame, catalytic functionality between the two different orientated LTON + catalyst samples is likely similar. Due to the similarity in the catalytic function of the nickel catalyst in both orientations, charge extraction due to catalytic function is unlikely to play a limiting role. Moreover, SEM images taken of the deposited catalyst show no discernible morphological difference (figure S4).

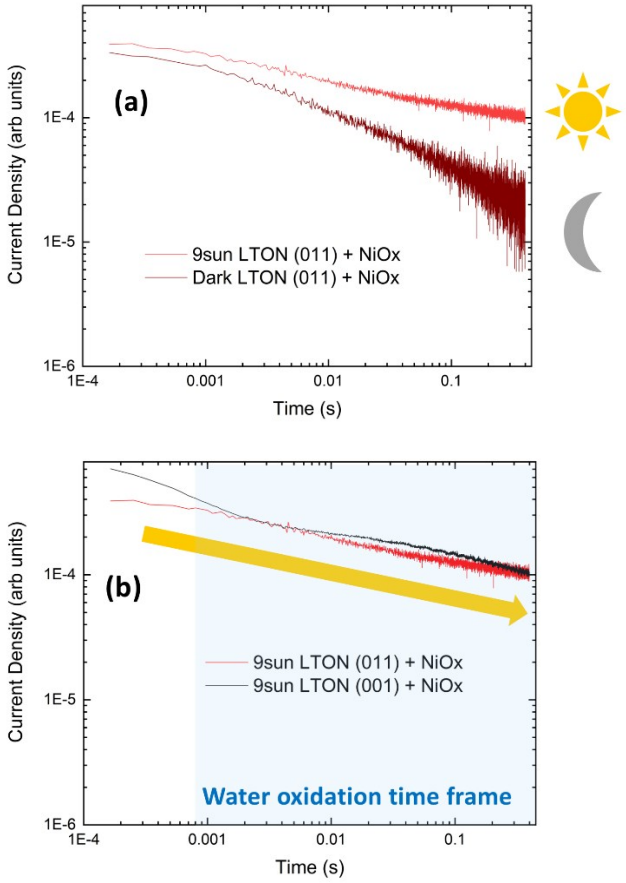

Figure 4. Charge decay curves from pulsed voltammetry measurements. Voltage is pulsed from 1.0V vs RHE to 1.3V vs RHE in pH 13.4 NaOH solution. a) Charge decay of LTON (011) + NiO_x with and without 9suns illumination. b) Charge decay of oriented LTON + NiO_x films under 9suns illumination.

Despite similar catalytic function, the presence of the NiO_x catalyst gives rise to unequal photocurrent improvements in different sample orientations. A photocurrent increase of over an order of magnitude is observed in both oriented LTON + catalyst films when compared to similarly applied voltages in the bare films but is noticeably larger in LTON (011)-NiO_x than in LTON (001)-NiO_x along all applied biases (figure 5). NiO_x deposition likely induces some light scattering effects which could increase absorption; however, since the amorphous NiO_x is not a semiconductor, it is unlikely to contribute directly to the photogeneration of charges.[32] Moreover, there is no observed wavelength dependent reflectivity in bare vs catalyst-decorated samples (figure S5); indicating that the overwhelming role of NiO_x is that of a catalyst – the light-scattering effects are not large enough to explain the order-of-magnitude increase in photocurrent observed in decorated LTON. In addition, photocurrent onset potentials shift towards more oxidative values for both orientations, indicating that photocharge extractability is improved upon addition of the nickel catalyst. This photocurrent onset is shifted towards even more oxidative potentials (red curve) in LTON (011)-NiO_x. Since less potential is required to extract charges in LTON (011)-NiO_x, this observation suggests that our LTON (011)-NiO_x sample may contain more mobile charges. Interestingly, photocurrent spikes flatten out in LTON (001)-NiO_x sample and indicate that nearly all extractable charges are scavenged. This is not the case in LTON (011)-NiO_x, where recombinative peaks are still visible and indicate a presence of excess extractable charges.

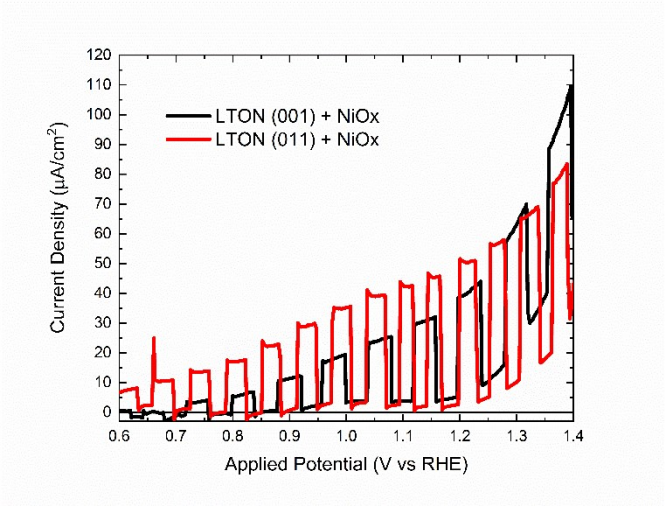

Figure 5. JV scans of oriented LTON films with NiO_x catalyst under chopped light illumination.

External quantum efficiency (EQE) measurements indicate that increased extraction of visible-light photocharges appears to be responsible for the large increase in scavengable charges in LTON (011)-NiO_x. EQE measurements of our LTON (011)-NiO_x and LTON (001)-NiO_x systems diverge only within the visible wavelength range (410 – 550 nm), but nearly completely overlap in all other (red and blue) ranges (figure 6a). Notably, this divergence in visible-light photocharge extraction accounts for a 30% increase in overall charge extraction between our catalyst-decorated oriented LTON samples (figure 6b). If we assume comparable charge generation in both orientations, these results support that the LTON (011) orientation induces greater visible-light photocharge mobility. Further, this increase in visible-light photocharge mobility is responsible for the large increase in LTON (011)-NiO_x photocurrent.

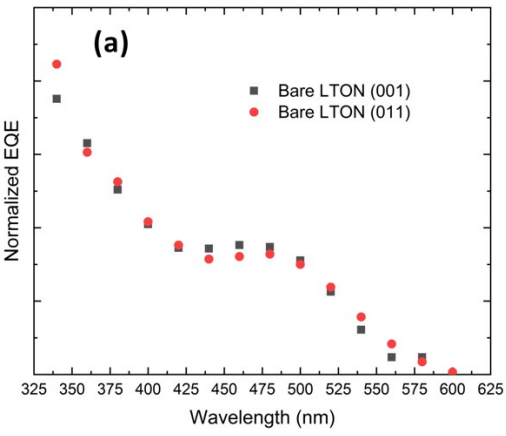

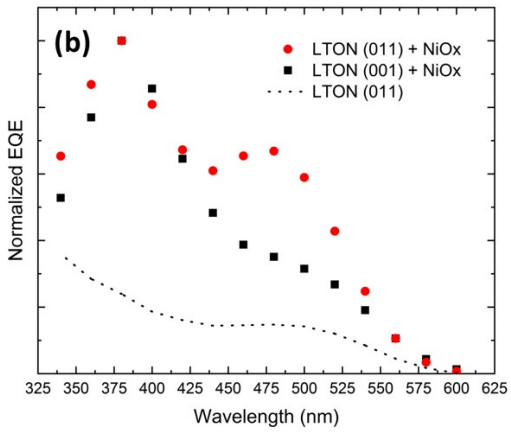

Figure 6. Normalized EQE curves of oriented LTON films with NiO_x catalyst under constant applied bias. a) normalized EQE of bare oriented LTON films b) normalized EQE of NiO_x decorated oriented thin films. The dashed line represents the bare LTON (011) film for facilitated comparison.

Separately, catalyst deposition also appears to induce additional differences to the shape of the EQE spectra. Both of our catalyst-decorated samples exhibit a peak at 375nm, while EQE spectra of our undecorated samples increase as a function of increasing incident light energy (with the highest EQE value at our last sampled wavelength of 325nm). Potentially, poor surface charge extraction in our bare samples favors the extraction of kinetically optimal higher energy charges.[33] A similar energetic explanation would also describe the general red-shift in the EQE spectra of both oriented catalyst samples – i.e. the presence of the nickel catalyst facilitates charge extraction of lower energy charges. Moreover, the dramatic changes in the spectral signature of our oriented LTON EQE spectra, from an unassuming superimposed spectrum to divergent spectra upon addition of catalyst further emphasizes the tremendous importance of the adequate surface charge extraction in understanding the full behavior of this material.

Computational results also indicate orientation-dependent charge carrier anisotropies in LTON. Density functional theory calculations were used to obtain the band structure of orthorhombic LTON with complete anion disorder (⅓ N and ⅔ O occupation on all anion sites) as modeled via the virtual crystal approximation. From the band structure shown in figure 7, we can see the direct bandgap at the Gamma point of the Brillouin zone (BZ), showing that under illumination with a wavelength just above the direct bandgap, most carriers will be generated around the Gamma point. Under illumination with shorter wavelengths, however, transitions at other points of the BZ can also contribute to optical absorption, and carriers can be generated at different wave vectors in the BZ.[34] Normally these hole carriers would decay towards the Gamma point via interaction with phonons, lowering their potential energy. If, however, charges are extracted more rapidly than this phonon-mediated decay, which with adequate catalysts is supported by both experiment and theory, they may retain the crystal momentum of the BZ point where they were generated.[35,36]

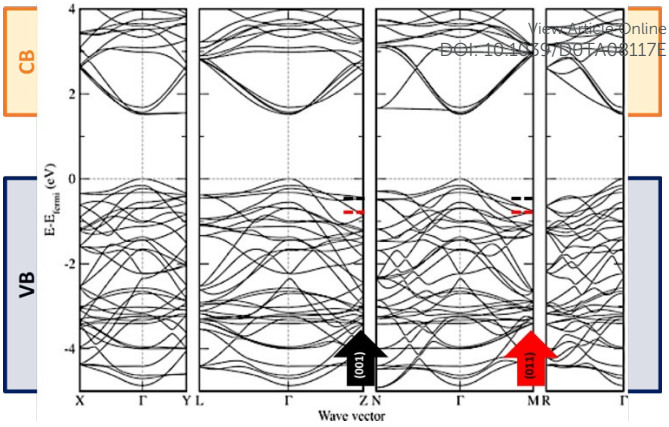

Figure 7. Computed band structure of orthorhombic LTON with anion disorder. The wave vectors corresponding to the (001) and (011) orientations are highlighted.

It is hence relevant to also consider hole carriers at points other than the Gamma point and in particular the M (011) and Z (001) directions corresponding to the predominant normal orientations of our experimental thin films. We see that the band energies of the highest valence bands are lower at the M compared to the Z point (dashed red and black line respectively in figure 7), resulting in holes with higher potential energy thus, if extracted before scattering by phonons, having a higher driving force for oxidation reactions. Moreover, we computed the band curvatures at these two points, which indicate that holes at the M point have an effective mass of 0.15 m_e, whereas holes at the Z point have an effective mass of 0.62 m_e. The lighter holes at the M point should hence be about 4-5 times more mobile than the heavier holes at the Z point. These results imply that electrons excited at the M point and extracted before phonon scattering have higher mobility and oxidation potential than their counterparts at the Z point. Our calculations also showed that these effects dominate over carrier numbers as the transitions at the M point contribute less to the absorption spectrum than transitions at the Z point. The latter thus provides a higher number of holes, which are however not as suitable to drive photochemical reactions. Ultimately, our computational results suggest that orientation control may offer a powerful technique to tune the performance in LTON via visible-light induced photocharge extraction.

Conclusion

Sufficient extraction of visible photocharges is necessary in order to overcome the efficiency barriers blocking the realization of solar fuel application. In our work, we clearly separate surface and bulk charge transfer bottlenecks and demonstrate that bulk orientation alone plays a driving role in the extraction of visible photocharges in LTON films. Moreover, we note that without proper hole extraction, surface charge extraction bottlenecks may mask bulk properties; only upon the addition of our NiO_x catalyst do we see the clear photocurrent and wavelength-dependent charge extraction differences due to bulk orientation among the studied LTON orientations. Our work uncovers a dramatic 30% increase in visible photocharge extraction via tuning the bulk crystallographic orientation in LTON films. As prior research also supports, crystallographic anisotropies likely have a considerable effect on charge extraction in additional photoelectrochemical materials.[3,4,37] However, in order to accurately quantify the effect any

crystallographic feature may have, care must be made in ensuring that bulk and surface effects are clearly identified and separated.

Conflicts of interest

There are no conflicts to declare.

Acknowledgements

The authors would like to thank the Paul Scherrer Institut and SNSF for their generous funding and particularly recognize SNSF grant no. 200020_172708 which directly funded this project. UA was support by a SNSF Professorship PP00P2_157615 and PP00P2_187185. Calculations were performed on UBELIX (http://www.id.unibe.ch/hpc), the HPC cluster at the University of Bern.

Notes and references

1 N. S. Lewis, *Science*, 2016, **351,** DOI:10.1126/science.aad1920.

2 N. Armaroli and V. Balzani, *Chem. - A Eur. J.*, 2016, **22**, 32–57.

3 J. Song, M. J. Seo, T. H. Lee, Y.-R. Jo, J. Lee, T. L. Kim, S.-Y. Kim, S.-M. Kim, S. Y. Jeong, H. An, S. Kim, B. H. Lee, D. Lee, H. W. Jang, B.-J. Kim and S. Lee, *ACS Catal.*, 2018, **8**, 5952–5962.

4 D. Li, Y. Liu, W. Shi, C. Shao, S. Wang, C. Ding, T. Liu, F. Fan, J. Shi and C. Li, *ACS Energy Lett.*, 2019, **4**, 825–831.

5 H. S. Han, S. Shin, D. H. Kim, I. J. Park, J. S. Kim, P. S. Huang, J. K. Lee, I. S. Cho and X. Zheng, *Energy Environ. Sci.*, 2018, **11**, 1299–1306.

6 S. C. Warren, K. Voïtchovsky, H. Dotan, C. M. Leroy, M. Cornuz, F. Stellacci, C. Hébert, A. Rothschild and M. Grätzel, *Nat. Mater.*, 2013, **12**, 842–849.

7 D. A. Grave, D. Klotz, A. Kay, H. Dotan, B. Gupta, I. Visoly-Fisher and A. Rothschild, *J. Phys. Chem. C*, 2016, **120**, 28961–28970.

8 M. Pichler, W. Si, F. Haydous, H. Téllez, J. Druce, E. Fabbri, M. El Kazzi, M. Döbeli, S. Ninova, U. Aschauer, A. Wokaun, D. Pergolesi and T. Lippert, *Adv. Funct. Mater.*, , DOI:10.1002/adfm.201605690.

9 M. Matsukawa, R. Ishikawa, T. Hisatomi, Y. Moriya, N. Shibata, J. Kubota, Y. Ikuhara and K. Domen, *Nano Lett.*, 2014, **14**, 1038–1041.

10 A. Kasahara, K. Nukumizu, T. Takata, J. N. Kondo, M. Hara, H. Kobayashi and K. Domen, *J. Phys. Chem. B*, 2003, **103**, 791–797.

11 J. Feng, W. Luo, T. Fang, H. Lv, Z. Wang, J. Gao, W. Liu, T. Yu, Z. Li and Z. Zou, *Adv. Funct. Mater.*, 2014, **24**, 3535–3542.

12 T. Minegishi, N. Nishimura, J. Kubota and K. Domen, *Chem. Sci.*, 2013, **4**, 1120.

13 C. C. L. Mccrory, S. Jung, I. M. Ferrer, S. M. Chatman, J. C. Peters and T. F. Jaramillo, *J. Am. Chem. Soc*, 2015, **137**, 4347–3457.

14 W. Si, D. Pergolesi, F. Haydous, A. Fluri, A. Wokaun and T. Lippert, *Phys. Chem. Chem. Phys. Phys. Chem. Chem. Phys*, 2017, **656**, 656–662.

15 M. W. Kanan and D. G. Nocera, *Science*, 2008, **321**, 1072–5.

16 G. Kresse, *J. Non. Cryst. Solids*, 1995, **192**–**193**, 222–229.

17 G. Kresse and J. Hafner, *Phys. Rev. B*, 1994, **49**, 14251–14269.

18 G. Kresse and J. Furthmüller, *Comput. Mater. Sci.*, 1996, **6**, 15–50.

19 G. Kresse and J. Furthmüller, *Phys. Rev. B - Condens. Matter Mater. Phys.*, 1996, **54**, 11169–11186.

20 J. P. Perdew, A. Ruzsinszky, G. I. Csonka, O. A. Vydrov, G. E. Scuseria, L. A. Constantin, X. Zhou and K. Burke, *Phys. Rev. Lett.*, 2008, **100**, 136406.

21 D. Joubert, *Phys. Rev. B - Condens. Matter Mater. Phys.*, 1999, **59**, 1758–1775.

22 P. E. Blöchl, *Phys. Rev. B*, 1994, **50**, 17953–17979.

23 H. J. Monkhorst and J. D. Pack, *Phys. Rev. B*, 1976, **13**, 5188–5192.

24 A. Fonari and C. Sutton, 2012.

25 M. Gajdoš, K. Hummer, G. Kresse, J. Furthmüller and F. Bechstedt, *Phys. Rev. B - Condens. Matter Mater. Phys.*, 2006, **73**, 045112.

26 S. P. Ong, W. D. Richards, A. Jain, G. Hautier, M. Kocher, S. Cholia, D. Gunter, V. L. Chevrier, K. A. Persson and G. Ceder, *Comput. Mater. Sci.*, 2013, **68**, 314–319.

27 M. Pichler, D. Pergolesi, S. Landsmann, V. Chawla, J. Michler, M. Döbeli, A. Wokaun and T. Lippert, *Appl. Surf. Sci.*, 2016, **369**, 67–75.

28 F. Haydous, M. Döbeli, W. Si, F. Waag, F. Li, E. Pomjakushina, A. Wokaun, B. Gökce, D. Pergolesi and T. Lippert, *ACS Appl. Energy Mater.*, 2019, **2**, 754–763.

29 C. Le Paven-Thivet, A. Ishikawa, A. Ziani, L. Le Gendre, M. Yoshida, J. Kubota, F. Tessier and K. Domen, *J. Phys. Chem C*, 2009, **113**, 6156-6162.

30 L. Mu, Y. Zhao, A. Li, S. Wang, Z. Wang, J. Yang, Y. Wang, T. Liu, R. Chen, J. Zhu, F. Fan, R. Li and C. Li, *Energy Environ. Sci.*, 2016, **9**, 2463–2469.

31 M. Matsukawa, R. Ishikawa, T. Hisatomi, Y. Moriya, N. Shibata, J. Kubota, Y. Ikuhara and K. Domen, *Nano Lett.*, 2014, **14**, 1038–1041.

32 J. Yu, S. Wang, B. Cheng, Z. Lin and F. Huang, *Catal. Sci. Technol.*, 2013, **3**, 1782–1789.

33 R. B. Singh, H. Matsuzaki, Y. Suzuki, K. Seki, T. Minegishi, T. Hisatomi, K. Domen and A. Furube, *J. Am. Chem. Soc.*, 2014, **136**, 17324–17331.

34 J. L. Giocondi, P. A. Salvador and G. S. Rohrer, *Top. Catal.*, 2007, **44**, 529–533.

35 R. B. Singh, H. Matsuzaki, Y. Suzuki, K. Seki, T. Minegishi, T. Hisatomi, K. Domen and A. Furube, *J. Am. Chem. Soc.*, 2014, **136**, 17324–17331.

36 A. Yamakata, M. Kawaguchi, N. Nishimura, T. Minegishi, J. Kubota and K. Domen, *J. Phys. Chem. C*, 2014, **118**, 23897–23906.

37 S. Kment, P. Schmuki, Z. Hubicka, L. Machala, R. Kirchgeorg, N. Liu, L. Wang, K. Lee, J. Olejnicek, M. Cada, I. Gregora and R. Zboril, *ACS Nano*, 2015, **9**, 7113–7123.

View Article Online
DOI: 10.1039/D0TA08117E

View Article Online
DOI: 10.1039/D0TA08117E

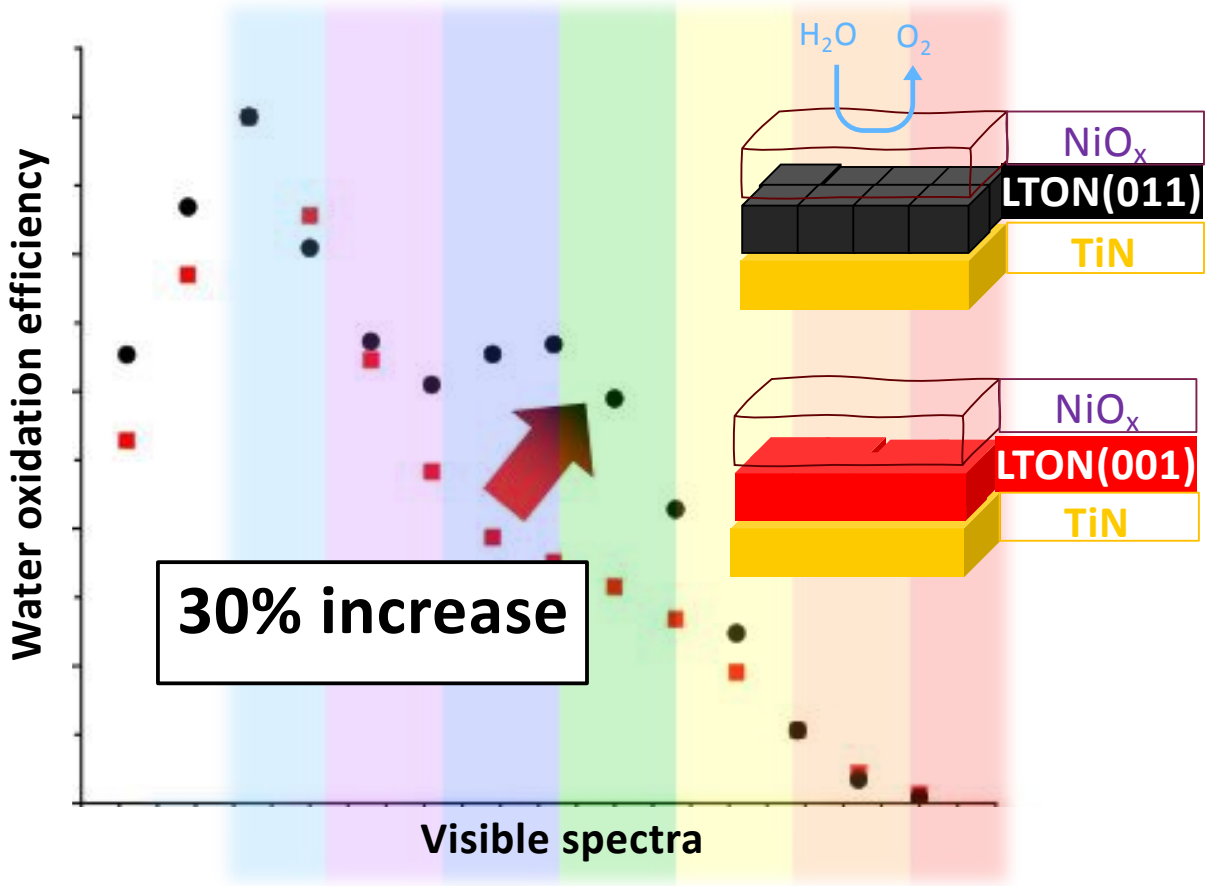

Visible-light induced photocharge extraction in $LaTiO_2N$ photoanodes increases by a significant 30% between (001) and (011) oriented thin-film samples